

## Article

# Baloxavir Marboxil Polymorphs: Investigating the Influence of Molecule Packing on the Dissolution Behavior

Xinbo Zhou <sup>1</sup>, Kaxi Yu <sup>2</sup>, Jiyong Liu <sup>2</sup> , Zhiping Jin <sup>1</sup> and Xiurong Hu <sup>2,\*</sup>

<sup>1</sup> Zhejiang Jingxin Pharmaceutical Co., Ltd., Shaoxing 312500, China; xinbo.zhou@jingxinpharm.com (X.Z.); hechengsuo@jingxinpharm.com (Z.J.)

<sup>2</sup> Department of Chemistry, Zhejiang University, Hangzhou 310027, China; yukaxi@zju.edu.cn (K.Y.); liujy@zju.edu.cn (J.L.)

\* Correspondence: huxiurong@zju.edu.cn; Tel.: +86-0571-8827-3491

**Abstract:** Baloxavir marboxil (BXM) is a new blockbuster FDA-approved anti-influenza virus agent. However, its poor solubility has limited its oral bioavailability. In this study, BXM was crystallized from several organic solvents, obtaining three polymorphs, and their dissolution behaviors were studied. Detailed crystallographic examination revealed that Form I is monoclinic, space group  $P2_1$ , with unit cell parameters  $a = 7.1159$  (3) Å,  $b = 20.1967$  (8) Å,  $c = 9.4878$  (4) Å,  $\beta = 109.033$  (1)°,  $V = 1289.02$  (9) Å<sup>3</sup>, and  $Z = 2$ , and Form II is monoclinic, space group  $P2_1$ , with unit cell parameters  $a = 7.1002$  (14) Å,  $b = 39.310$  (7) Å,  $c = 9.7808$  (18) Å,  $\beta = 110.966$  (5)°,  $V = 2549.2$  (8) Å<sup>3</sup>, and  $Z = 4$ . Form I has a rectangular three-dimensional energy frameworks net, while Form II has a two-dimensional net. On the other hand, Form II has a much larger percentage of its surface area of exposed hydrogen bond acceptors than Form I. These crystallographic features offered increased solubility and dissolution rate to Form II. The results of stability and solubility experiments suggest that Form II may be preferred in the solid form used for the industrial preparation of BXM medicinal products.



**Citation:** Zhou, X.; Yu, K.; Liu, J.; Jin, Z.; Hu, X. Baloxavir Marboxil Polymorphs: Investigating the Influence of Molecule Packing on the Dissolution Behavior. *Crystals* **2022**, *12*, 550. <https://doi.org/10.3390/cryst12040550>

Academic Editors: Jingxiang Yang, Xin Huang and Duane Choquesillo-Lazarte

Received: 22 March 2022

Accepted: 13 April 2022

Published: 15 April 2022

**Publisher's Note:** MDPI stays neutral with regard to jurisdictional claims in published maps and institutional affiliations.



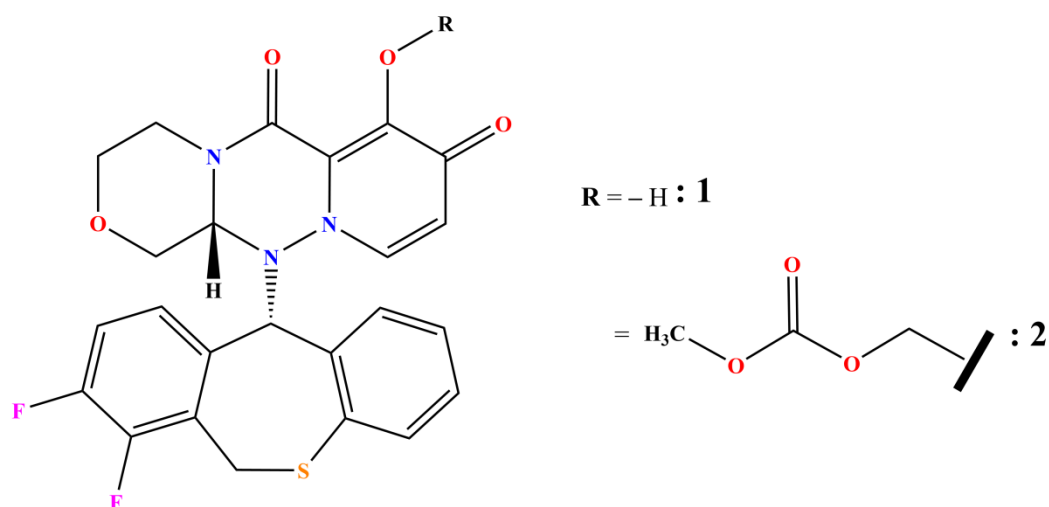
**Copyright:** © 2022 by the authors. Licensee MDPI, Basel, Switzerland. This article is an open access article distributed under the terms and conditions of the Creative Commons Attribution (CC BY) license (<https://creativecommons.org/licenses/by/4.0/>).

**Keywords:** baloxavir marboxil; crystallization; polymorphism; crystal structure; energy framework; solubility

## 1. Introduction

Epidemic and pandemic influenza is a contagious respiratory illness caused by influenza viruses and has become a major public health concern [1,2]. Treatment of influenza has relied heavily on neuraminidase (NA) inhibitors, which target the viral neuraminidase activity of the NA protein [3].

Fortunately, in 2018, baloxavir marboxil (abbreviated as BXM, Scheme 1) was developed as a first in class, orally active, cap-dependent endonuclease inhibitor, which has a unique mechanism of action when compared with the currently existing neuraminidase inhibitor drug class used to treat influenza infections [4,5]. BXM is a prodrug that is metabolized into the active baloxavir acid (BXA, Scheme 1) and directly inhibits the cap-dependent endonuclease activity of the polymerase acidic protein of influenza A and B viruses [6]. The drug was approved in Japan and other countries, including the U.S., and marked under the brand name Xofluza [7–9]. This is the first new antiviral flu treatment with a novel mechanism of action approved by the FDA in nearly 20 years [7]. Recent studies by experimental and computational techniques indicate that BXM is a valuable candidate treatment for human patients suffering from the highly pathogenic H7N9 virus, H3N2 virus, and COVID-19 virus infection [10–13]. However, BXM is insoluble in an aqueous medium in its crystalline form, and its poor solubility has limited its oral bioavailability [14]. The average oral bioavailability of BXM was only approximately 14.7% [14–16].



**Scheme 1.** Chemical structure of baloxavir acid (BXA,1) and baloxavir marboxil (BXM, 2).

Polymorphism means the potential for a drug to form one or more crystalline solids that differ by the molecular arrangement of drug molecules in the crystal lattice [17,18]. Polymorphic forms of drugs that give a difference in thermodynamic and physicochemical properties, such as melting point, density, stability, and in particular, solubility, can offer an improvement/reduction on the original form [19–26]. The most notorious example of the impact of polymorphs on solubility and dissolution rate is the protease inhibitor Ritonavir [27]. Thus, the evaluation and application of polymorphs that are able to improve the solubility and dissolution rate of BXM are of paramount importance [26,28]. However, to the best of our knowledge, studies about its crystalline structures, morphology, thermodynamic stability, and dissolution properties have not yet been reported. Structure–property relationship is helpful in understanding the critical aspects during formulation development. Herein the study considers in depth the polymorphic forms of BXM with particular emphasis on their molecule packing, solubility, and the relationship between crystal packing and dissolution behavior.

## 2. Materials and Methods

### 2.1. Materials

Baloxavir marboxil (purity > 99.5%, Form I) was supplied by Zhejiang Jingxin Pharmaceutical Co., Ltd. (Shaoxing, China) and was used without further purification. All other solvents and chemicals were of analytical grade or chromatographic grade and were purchased from Shanghai Aladdin bio-chem technology company Ltd. (Shanghai, China), Sinopharm chemical reagent Co., Ltd. (Shanghai, China), Shanghai lingfeng chemical reagent Co., Ltd. (Shanghai, China) and used as received.

### 2.2. Methods

#### 2.2.1. BXM Polymorphs Preparation and Single Crystal Growth

Form I was prepared by recrystallization of BXM in methanol. In particular, 500 mg of BXM was dissolved in 35 mL of methanol, the solution was filtered, and slow cooling of the solution yielded Form I. For crystal structure determination, good quality crystals of Form I were produced by dissolving 20 mg of BXM in 10 mL methanol. Slow evaporation at 25 °C produced block crystals after approximately 1 week.

Form II was prepared from acetonitrile solution of BXM by adding n-heptane as an antisolvent. In particular, 500 mg of BXM was dissolved in 10 mL of acetonitrile, and the resultant clear solution cooled to 0 °C; 15 mL of n-heptane was dropped over 10 min. The prepared mixture became cloudy and then filtered. Crystals of Form II for crystal structure determination were produced by dissolving 20 mg of BXM in a mixture of 3 mL acetonitrile

and 7 mL n-heptane. Slow evaporation at 25 °C produced rod-like crystals after about 10 days.

Form III was prepared by recrystallization of BXM in ethyl acetate. In particular, 500 mg of BXM was dissolved in 50 mL of ethyl acetate. The prepared solution was then stirred and quickly cooled to 0 °C. The obtained cloudy solution was filtered. Unfortunately, slow crystallization in ethyl acetate does not result in Form III but in Form I.

#### 2.2.2. Crystal Habit Observation

Microscopic examination and photomicroscopy were performed using a Bresser microscope equipped with a CMOS camera. The sample was put on the objective glass and was examined directly, without cover glass.

#### 2.2.3. Powder X-ray Diffraction (PXRD)

The PXRD patterns were obtained on a Rigaku D/Max-2550PC diffractometer (Rigaku Co., Tokyo, Japan), using a CuK $\alpha$  X-ray radiation source ( $\lambda = 1.5418 \text{ \AA}$ ) and generator operated at 40 kV and 250 mA. The scans were run from 3.0 to 40.0° (2 $\theta$ ), with an increasing step size of 0.02° and a count time of 1 s.

#### 2.2.4. Differential Scanning Calorimetry (DSC)

The DSC analysis was performed on a TA DSC Q100 differential scanning calorimeter. Approximately 4–7 mg powder samples were placed in an aluminum pan, and the heating was carried out at a rate of 10 °C/min under a nitrogen flow of 50 mL/min. A temperature range of 25–250 °C was scanned. The data were managed using TAQ Series Advantage software 4.7 (Universal analysis 2000).

#### 2.2.5. Thermogravimetric Analysis (TGA)

TGA was performed on an SDT Q600 instrument from 25 °C to 450 °C, at a heating rate of 10 °C/min, and under nitrogen purge at a flow rate of 50 mL/min. The data were managed using TAQ Series Advantage software 4.7 (Universal analysis 2000).

#### 2.2.6. Single-Crystal X-ray Diffraction (SCXRD)

Single crystal X-ray diffraction data collection was performed on a Bruker Apex II CCD diffractometer (Karlsruhe, Germany) with Mo-K $\alpha$  radiation ( $\lambda = 0.71073 \text{ \AA}$ ). Integration and scaling of intensity data were accomplished using the SAINT V8.38A program [29]. The crystal structure was solved by direct methods using SHELXT [30] and refined by a full-matrix least-squares method with anisotropic thermal parameters for all non-hydrogen atoms on F2 using SHELXL [31] in Olex 2 [32]. Hydrogen atoms were placed in the position of metrically calculation or difference Fourier map and were refined isotropically using a riding model. Diamond and Olex 2 [32] were used to draw figures. The simulated PXRD pattern was calculated using Mercury [33]. The crystallographic data are listed in Table 1. Crystal structures are deposited as part of the supporting information and may be accessed at [www.ccdc.cam.ac.uk/data\\_request/cif](http://www.ccdc.cam.ac.uk/data_request/cif) (accessed on 22 March 2022, CCDC 2088906–2088907).

**Table 1.** Crystallographic data of Form I and II.

	Form I	Form II
Empirical formula	C <sub>27</sub> H <sub>23</sub> F <sub>2</sub> N <sub>3</sub> O <sub>7</sub> S	C <sub>27</sub> H <sub>23</sub> F <sub>2</sub> N <sub>3</sub> O <sub>7</sub> S
Formula weight	571.54	571.54
Temperature (K)	296	170
Crystal size (mm)	0.50 × 0.46 × 0.16	0.35 × 0.08 × 0.06
Crystal system	Monoclinic	Monoclinic
Space group	P2 <sub>1</sub>	P2 <sub>1</sub>
a (Å)	7.1159 (3)	7.1002 (14)
b (Å)	20.1967 (8)	39.310 (7)
c (Å)	9.4878 (4)	9.7808 (18)
β (°)	109.033 (1)	110.966 (5)
Volume (Å <sup>3</sup> )	1289.02 (9)	2549.2 (8)
Z	2	4
ρ <sub>calc</sub> g/cm <sup>3</sup>	1.473	1.489
μ (mm <sup>-1</sup> )	0.193	0.20
F (000)	592.0	1184
Reflections collected	19,783	26,198
Independent reflections (Rint)	5239 (0.023)	10,025 (0.052)
Data/restraints/parameters	5239/121/400	10,025/1/723
R <sub>1</sub> , wR <sub>2</sub> [I > 2_σ(I)]	0.0285, 0.0732	0.06650, 0.1608
R <sub>1</sub> , wR <sub>2</sub> [all data]	0.0293, 0.0739	0.0717, 0.1637
Goodness-of-fit on F <sup>2</sup>	1.05	1.19
Largest diff. peak/hole/e Å <sup>-3</sup>	0.17, −0.18	0.40, −0.34
Flack parameter	0.039 (18)	0.04 (3)
CCDC No.	2088906	2088907

### 2.2.7. Powder Dissolution Studies and Stability Tests

The powder dissolution experiments were carried out in pH 1.2 simulated gastric fluids (water was added to 2.0 g of sodium chloride in 7.0 mL of hydrochloride acid to reach 1000 mL). A series of known BMX concentrations in pH 1.2 simulated gastric fluids were prepared to generate a calibration curve. The powder dissolution experiments were carried out in a Tianda Tianfa Technology RC806D dissolution tester with a paddle rotation speed of 100 rpm at 37 °C. Precisely weighted samples (1.0 g) were added into the dissolution vessels with 900 mL pH 1.2 simulated gastric fluids. Prior to powder dissolution experiments, all solid-phase samples were sieved through a 300-mesh screen to eliminate the effect of size on the results. Five milliliters of the aliquot were collected at specific time intervals and filtered via an organic membrane (0.22 μm), and the concentration of the aliquots was determined with appropriate dilutions from the predetermined standard curves of the respective compounds. Moreover, the undissolved samples were collected after solubility experiments for measurement via PXRD. Three crystal forms were stored at 25 ± 2 °C and 60% RH ± 5% RH and then analyzed after 12 months of storage.

## 3. Results

### 3.1. Crystallization

According to the Q3C guideline for residual solvents [34], a systematic polymorph screening of BXM was performed by recrystallization from several organic solvents at variable conditions. The identity and purity of the prepared solid forms were verified by PXRD (Table S1 in the Supplementary Materials). Through the screening process, BXM was found to crystallize in three crystal forms, named 'Form I', 'Form II', and 'Form III'. Forms I and II, prepared by the solvent evaporation method, were crystallized and suitable for single-crystal X-ray diffraction analysis (Figure 1a,b). Despite all our efforts, the structure solution of Form III was not successful thus far because of the small size and poor quality of the crystals. Crystal size and quality were unable to be improved upon, as it was obtained only by stir precipitation (Figure 1c).

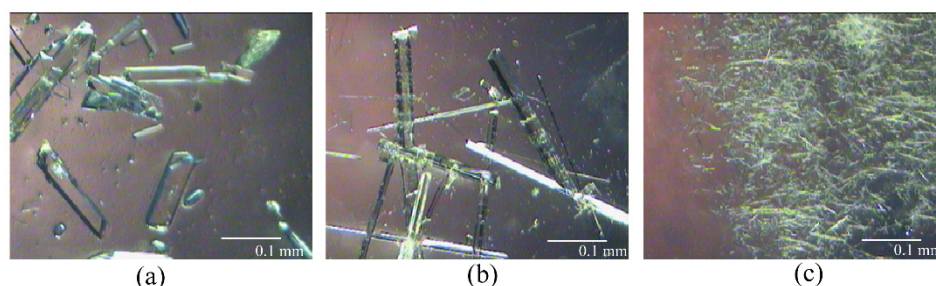


**Figure 1.** Photographs of (a) Form I, (b) Form II, and (c) Form III.

### 3.1.1. Crystal Structure of Form I and II

X-ray crystal structures were determined for Forms I and II, and their crystallographic parameters and structure refinement details are listed in Table 1. Forms I and II crystallized in a monoclinic crystal system and  $P2_1$  space group. Additionally, the asymmetric unit of I consisted of one BMX molecule (Figure 2a), while Form II contained two molecules (Figure 2b,c). Homochirality of the BMX molecules in both polymorphic forms had been determined from polarimetric data, all molecules having the S-configuration at C10 and the R-configuration at C15. The methymethyl carbonate chain displays positional disorder in the single crystal structure of Form I; these atoms were split into two positions, with site-occupation factors of 0.606(5):0.394(5). Overlaying the molecular conformations found in Form II with that of I shows that the only difference is the rotation of the methymethyl carbonate chain, while the other bonds overlay nicely (Figure 2d). This result indicates that the formation of different solid forms is not due to changes in molecular conformation.

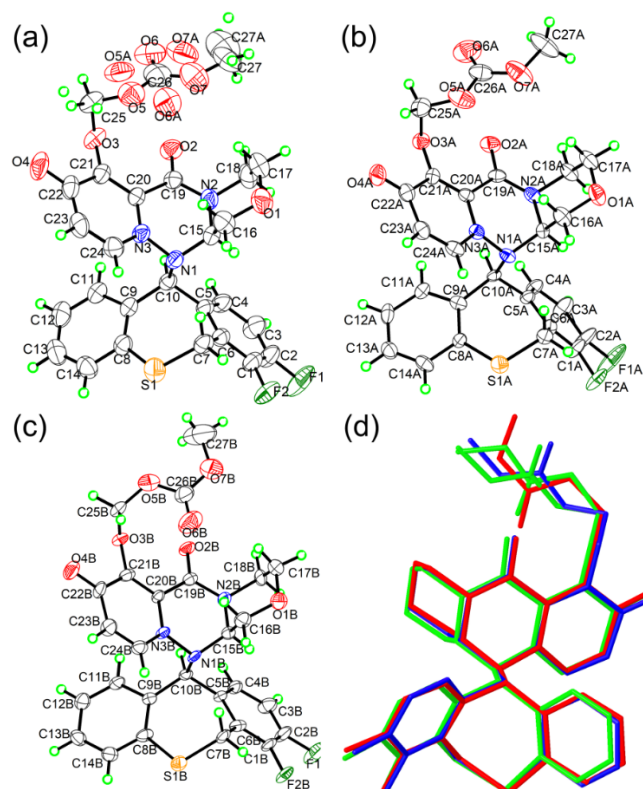


**Figure 2.** The ORTEP figures of (a) Form I, (b) molecule A of Form II, and (c) molecule B of Form II drawn at the 50% probability level. H atoms are shown as small spheres at a 0.15 Å radius. (d) Superposition of the BXM in I (green), molecule A (red), and molecule B (blue) in II. Hydrogen atoms were omitted for clarity.

Since the absence of a typical O-H or N-H donor but with 10 hydrogen bond acceptors in the BXM molecule, the formation of crystal packing arrangement for BXM is governed by a network of nonclassic hydrogen bonds. In the crystal structure of Form I, BXM molecules are linked via  $C(sp^3)\text{-H} \dots \text{O}$  and  $C(sp^2)\text{-H} \dots \text{F}$  interactions, which develop into a one-dimensional chain and run parallel to the  $c$ -axis, as shown in Figure 3a and Table S2. Neighboring chains are then packed head-to-tail via short contacts in the  $bc$  plane (Figure 3c). The major intermolecular interaction between molecules in Form II is a  $C(sp^2)\text{-H} \dots \text{F}$  hydrogen bond, as shown in Figure 3b and Table S3. The major difference from Form I is the relative orientation of adjacent chains stacking. In Form II, the neighboring chains are packed head-to-head via  $C(sp)\text{-H} \dots \pi$  interactions between aromatic rings, forming a hydrogen-bonded bilayered structure (Figure 3d). Additionally, auxiliary  $C(sp^3)\text{-H} \dots \text{O}$  interactions are also contributing to the stability of the crystal structure in both polymorphs. In order to visualize and quantify the similarities/dissimilarities of intermolecular contacts in two polymorphs, Hirshfeld surface analysis [35,36] was calculated with the aid of CrystalExplorer 17.5 [37]. The results were visualized in the two-dimensional fingerprint plots, and there is no significant difference between the % distributions in different interactions (Figure S1 in the Supplementary Materials).

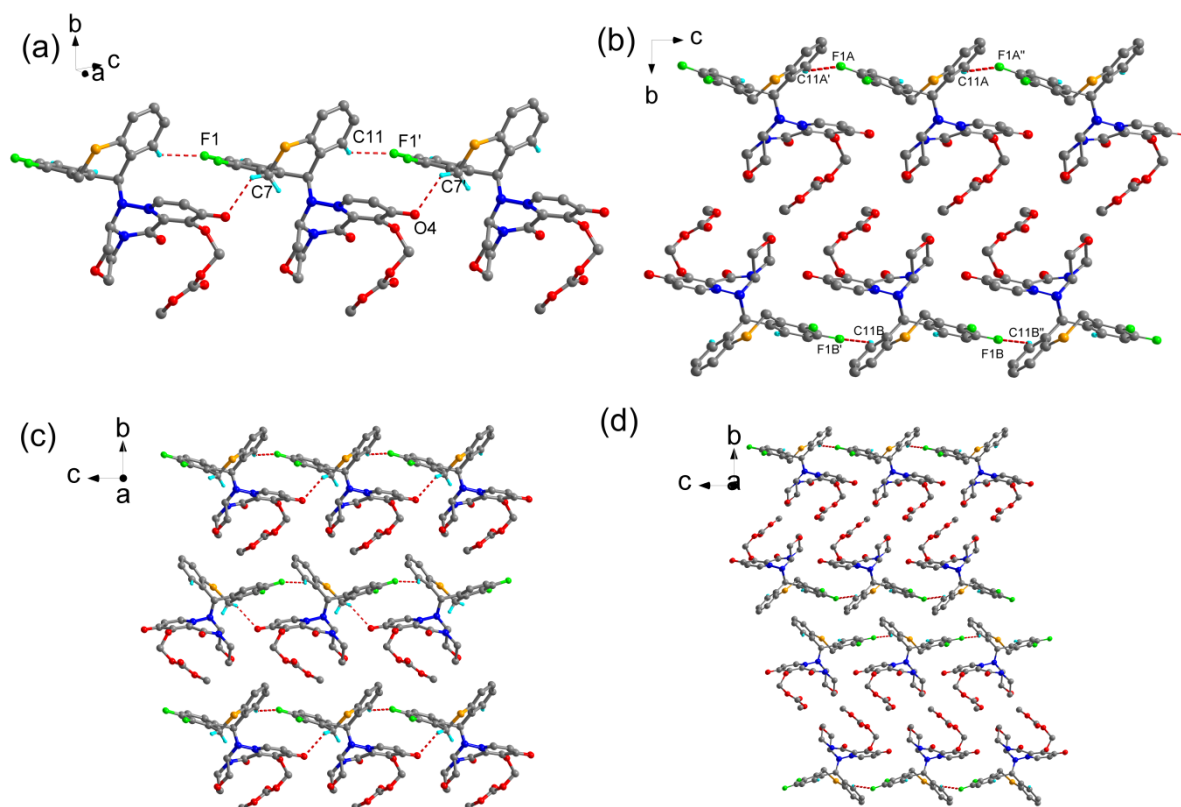


**Figure 3.** (a) 1D chain constructed by  $C11\text{-H}11 \dots \text{F}1$  and  $C7\text{-H}7\text{B} \dots \text{O}4$  interactions run parallel to the  $c$ -axis in Form I; (b) 1D chain constructed by  $C11\text{-H}11 \dots \text{F}1$  interactions run parallel to the  $c$ -axis in Form II; (c) view of the three-dimensional packing of Form I (viewed along the  $a$ -axis direction); (d) view of the three-dimensional packing of Form II (viewed along the  $a$ -axis direction).

### 3.1.2. PXRD

The excellent accordance between the experimental and crystal structure simulated PXRD patterns of Form I and II corroborated the identity of the precipitated powder (Figure 4). The major characteristic PXRD peaks of Form I appear at  $2\theta$  values of  $8.7^\circ$ ,  $10.8^\circ$ ,  $14.3^\circ$ ,  $17.5^\circ$ ,  $21.6^\circ$ ,  $24.1^\circ$ ,  $26.4^\circ$ , and  $29.7^\circ$ . Form II showed the peaks at  $2\theta$  values of  $4.4^\circ$ ,  $8.9^\circ$ ,  $11.7^\circ$ ,  $14.0^\circ$ ,  $17.8^\circ$ ,  $22.3^\circ$ ,  $24.3^\circ$ , and the characteristic peaks of Form III are at  $2\theta$  values

of  $4.3^\circ$ ,  $8.7^\circ$ ,  $10.6^\circ$ ,  $13.4^\circ$ ,  $17.1^\circ$ , and  $22.0^\circ$ . Specifically, Form II has distinctive peaks at  $11.7^\circ$ ,  $14.0^\circ$ ,  $22.3^\circ$ , and  $24.3^\circ$  that are absent in Form III (Figure S2).

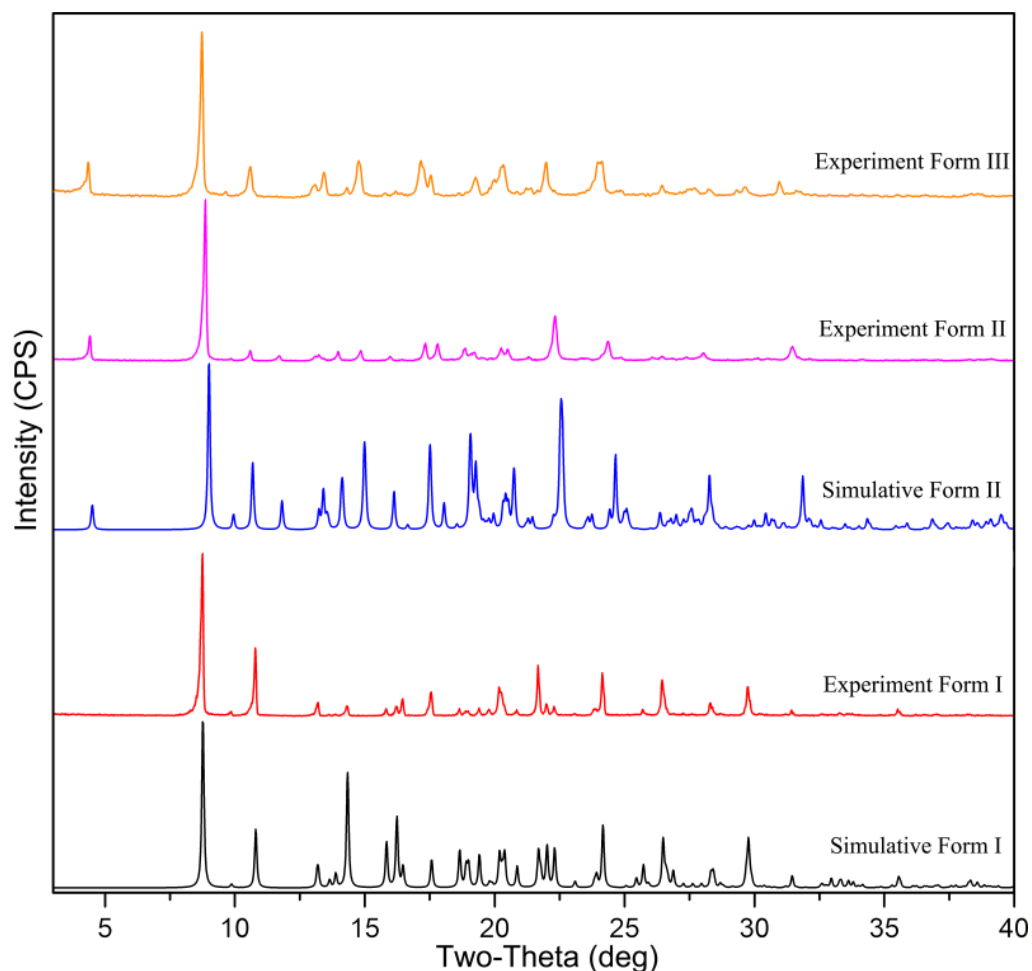


**Figure 4.** PXRD patterns of all here described solid forms of BXM.

### 3.1.3. TGA-DSC

To evaluate the thermal properties of the prepared solids, we performed DSC and TGA measurements. As shown in Figure 5, the DSC curve of Form I exhibited two thermal events: a small endothermic event at  $230.4^\circ\text{C}$  followed by a sharply defined melting event at  $238.7^\circ\text{C}$ . The first endothermic peak was associated with a phase change since there was no mass loss in this temperature range. The second one resulted from the melting of the obtained solid in the phase transition process. DSC curve of Form II and III shows stability up to approximately  $235.5^\circ\text{C}$  and  $238.7^\circ\text{C}$ , respectively. The DSC thermal analysis shows that three polymorphs exhibit an explosive type of degradation at melting, which is accompanied by a large release of heat. The melting was irreversible and resulted in a dark-brown tar. The TGA curve exhibits no weight loss until decomposition, which proves all three polymorphs are in anhydrate form (Figure S3).

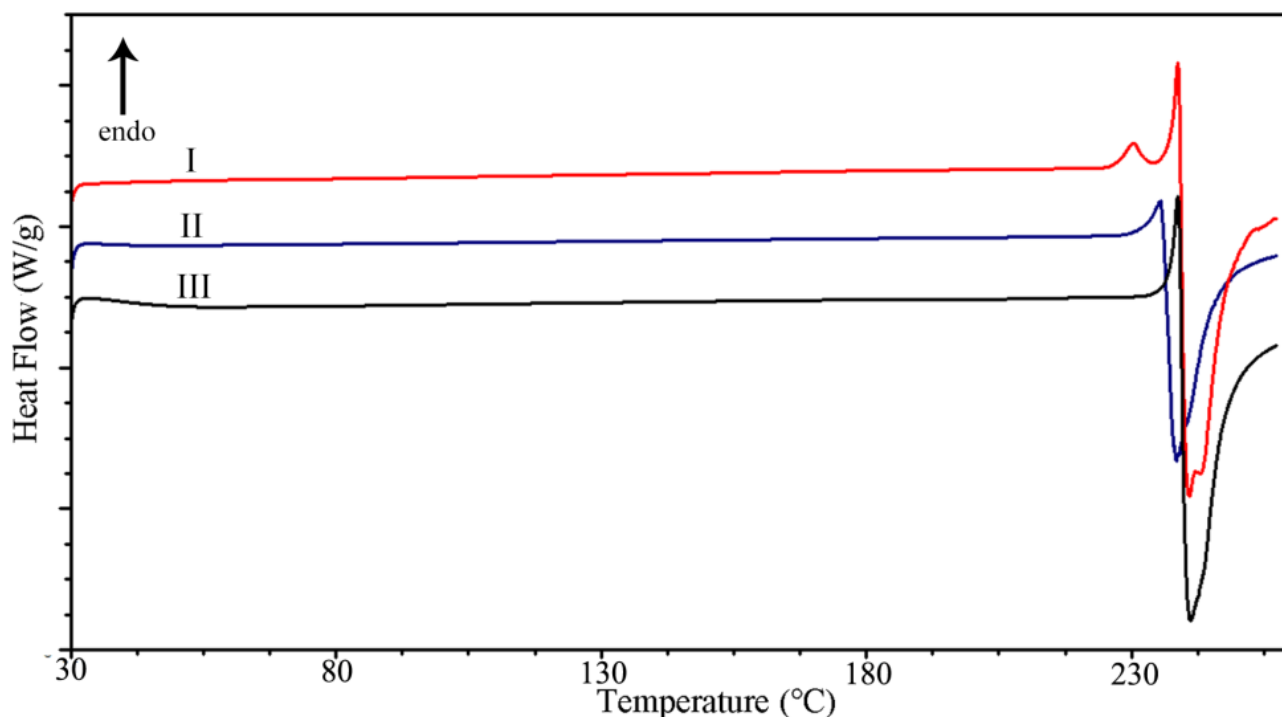


**Figure 5.** DSC curves of BXM in Form I, Form II, and Form III at a 10 °C/min heating rate.

### 3.2. Dissolution Profile of Polymorph and Stability

The powder dissolution behaviors of the BXM polymorphs determined in pH 1.2 simulated gastric fluids at 37 °C are demonstrated in Figure 6. Form III was dissolved faster than Form I and II at the first stage. After 10 min, the solubility of Form III displays a “spring and parachute” effect [38]. With increasing time, BXM concentration in solution decreases, and after 40 min, the concentration is close to that of Form I, indicating that the precipitation process (Form I) is happening, and Form III converts into less soluble Form I under suspension condition. In addition, Form II presents an extreme increase in solubility when compared with Form I. The  $S_{\max}$  values of II and III are 1.4 and 1.3 times as high as that of Form I. After the dissolution study, the remaining solid phase was characterized by PXRD analysis (Figure S10). It was confirmed that Form III almost converted to Form I as expected, while Form I and II retained their respective crystal forms, and there is no change even if suspended in water for seven days. The equilibrium solubility of Form I and II was  $21.2 \pm 0.2$  and  $29.4 \pm 0.4$   $\mu\text{g/mL}$ , respectively. All three polymorphs have been shown to be as stable on the shelf for 12 months under the conditions of  $25 \pm 2$  °C and 60% RH  $\pm$  5% RH (relative humidity) (Figure S11). The particle size is an important factor in the dissolution behavior of the API [39]. Therefore, to exclude the impact of particle size on the dissolution, crystals of a similar size range were used in the experiment. Thus, the difference in dissolution behavior between BXM polymorphs, especially for Form I and II, is due to the differences in the molecule packing rather than the particle size of the material studied.

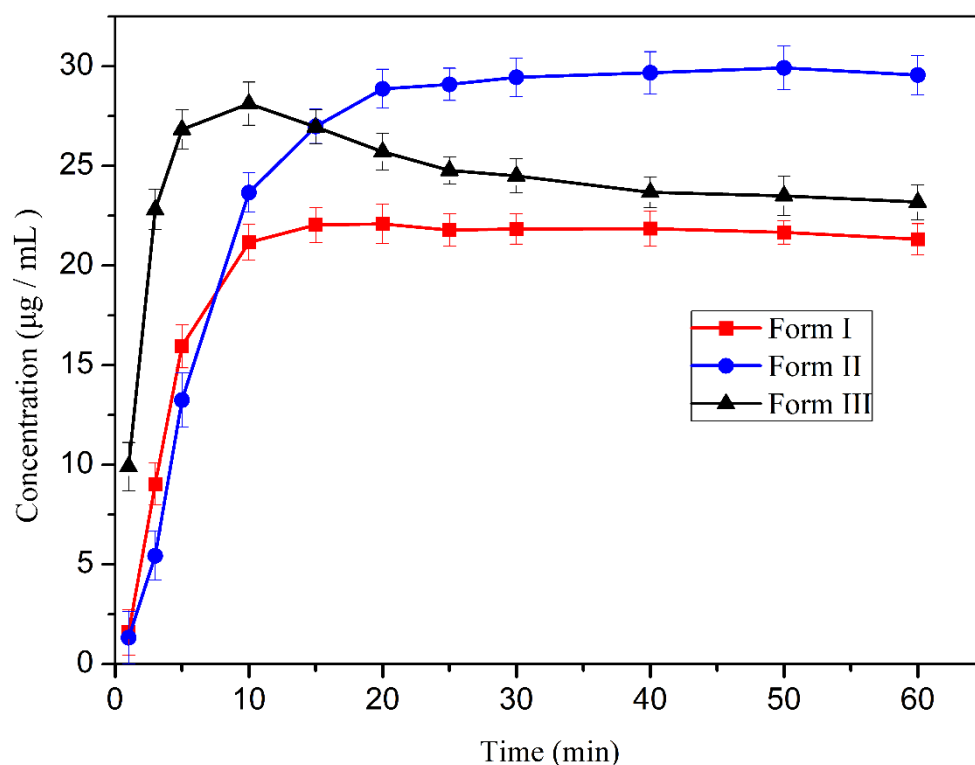


**Figure 6.** Powder dissolution profiles of BXM Form I, II, and III in pH 1.2 simulated gastric fluids at 37 °C. Data were shown as mean  $\pm$  SD ( $n = 3$ ).

#### 4. Discussion

There has been an increasing interest in the correlations between the crystal structure, crystal morphology, and physicochemical properties of an investigational pharmaceutical compound [22,40]. Crystal morphology plays an important role in the dissolution behavior of drugs, depending on the functional groups exposed on the surface [41–43]. The theoretical crystal morphology of Form I and II was simulated by the Bravais-Friedel-Donnay-Harker (BFDH) model and growth morphology (GM) models with the aid of Materials Studio [38] (Figure 7, Table S4). By comparing Figures 7 and 1a,b, it can be seen that the simulated morphologies are similar to the crystal habit of the experimentally obtained crystals, but there are still some differences because the simulated morphologies only predict the crystal habit from the perspective of the internal structure of the crystal itself and do not consider the influence of the external environment on the crystal growth. The crystal habit obtained in the actual crystallization process is simultaneously affected by the combined effects of thermodynamics and kinetics. Therefore, the actual crystal habit obtained under different crystallization conditions may be different from the theoretical crystal habit calculated by the model. Vacuum morphology of Form I and II was generated by the BFDH model. The benefit of this method was to identify important faces in the growth process [44]. Results show that (0–20), (001), (0–11), and (100) are among the major surfaces, with (0–20) being the most dominant face. The calculated aspect ratio by BFDH morphology for Form I and II was 1.778 and 3.254, respectively. Surface structures of all important facets of Form I and II given by the MG model were studied. For Form I, (0–20) occupies 35% of the surface area and exhibits an attachment energy ( $E_{att}$ ) value of  $-47.906$  kcal/mol, while for Form II, (0–20) occupies 62% of the surface area and exhibits an  $E_{att}$  value of  $-31.244$  kcal/mol. Because of the structural dissimilarity as described earlier, the orientation of molecules on the exterior of each facet of a crystal was diverse. For Form I, the (0–20) facet has a bed of phenyl moieties, making it relatively more hydrophobic (Figures 8 and S4), while, in Form II, the exposure of methymethyl carbonate chain makes it more hydrophilic (Figures 8 and S5). Thus Form II has a much greater percentage of



To further understand the relationship between crystal packing and dissolution behavior, energy frameworks were generated to visualize the differences in the supramolecular architecture of Form I and II in terms of energetics [47,48]. CrystalExplorer 3.1 [37] was used to construct energy frameworks at the B97D/6-31G\*\* level of theory [47,49]. For Form I, energy bonds are evenly distributed over the whole structure such that they make a rectangular three-dimensional net (Figure S6, Table S5), while, in Form II, the energy bonds are ordered between aromatic rings such that they make rectangular two-dimensional layers (Figure S7, Table S6). The energy frameworks suggest relatively weaker interactions between the layers in Form II. The methymethyl carbonate segment of BXM oriented right and left the energy layers, rendering the surface of the layers hydrophilic. The progress of the dissolution requires easily accessible hydrophilic groups after the initially exposed groups have dissolved. For Form II, after one layer of BXM molecules is dissolved, the subsequent layers are more easily split along the b-axis due to no energy bonds between layers. In addition, the stripped bilayer surface covered hydrophilic groups. This result may also account for the higher solubility of Form II.

## 5. Conclusions

In this contribution, we prepared and characterized the solid-state behavior of the polymorphs of BXM. Three polymorphs have chemically the same building blocks, but their dissolution behaviors differ significantly. The only difference which can be related to the observed change in the dissolution behaviors is their significantly different packing features. The crystal structure of Form I and II were identified by SXRD. Using the crystal structure data, we confirmed that Form I contains strong energy bonds between the molecular layers, while in Form II, there are no energy bonds observed between the layers. Moreover, the theoretical crystal habits of Form I and II show that Form II has a much greater percentage of its surface area with exposed hydrogen bond acceptors than Form I. The results of stability and solubility experiments suggest that Form II may be a preferred solid form.

**Supplementary Materials:** The following are available online at <https://www.mdpi.com/article/10.3390/cryst12040550/s1>, Table S1: screening of BXM crystal form (Part of the experimental process), Table S2: Hydrogen bonds geometry (Å, °) for Form I, Table S3: Hydrogen-bond geometry (Å, °) for Form II, Figure S1: 2D fingerprint plots of the Hirshfeld surfaces for components of BXM Form I and II, Figure S2: showing the comparison of observed PXRD patterns of Form II and III. The variations in peak positions across the polymorphs are pointed by the arrows, Figure S3: TG curves of BXM in I, II, and III at a 10°C/min heating rate, Table S4: morphology predictions for Form I and II by means of BFDH and GM calculations, Figure S4: crystal slices of different facets of BXM Form I expressing the presence of functional groups. The most dominant facet (020) is covered by 1 phenyl, and the second dominant facet (001) is covered by 1 carbonyl, Figure S5: crystal slices of different facets of BXM Form II expressing the presence of functional groups. The most dominant facet (020) is covered by 1 methoxyl, and the second dominant facet (001) is covered by 2 fluorines, 2 carbonyl, and 1 methymethyl carbonate chain, Figure S6: energy frameworks corresponding to the different energy components and the total interaction energy in BXM Form I, Figure S7: energy frameworks corresponding to the different energy components and the total interaction energy in BXM Form II, Figure S8: color coding for the neighboring molecules around a molecule of BXM Form I. The molecule is shown with atom type color, Figure S9: color coding for the neighboring molecules around molecule A (top) and molecule B (bottom) of BXM Form II. The molecules are shown with atom type color, Table S5: molecular pairs and the interaction energies (kJ/mole) obtained from energy framework calculation for BXM Form I, Table S6: molecular pairs and the interaction energies (kJ/mole) obtained from energy framework calculation for BXM Form II, Figure S10: the PXRD pattern of the source BXM, Figure S11: Stability of Form I, Form II and Form III after storage of 12 months at 25 ± 2 °C and 60% RH ± 5% R shown in the PXRD pattern.

**Author Contributions:** Conceptualization, X.Z. and X.H.; software, K.Y. and X.Z.; Single-crystal XRD measurement, structure solution, and refinement, J.L.; writing—original draft preparation, X.Z.; writing—review and editing, X.Z. and X.H.; supervision, X.H. and Z.J. All authors have read and agreed to the published version of the manuscript.

**Funding:** This research received no external funding.

**Institutional Review Board Statement:** Not applicable.

**Informed Consent Statement:** Not applicable.

**Data Availability Statement:** Not applicable.

**Acknowledgments:** The authors thank Linshen Chen of Zhejiang University for his help with the TG/DSC measurements and analyses.

**Conflicts of Interest:** The authors declare no conflict of interest.

## References

1. Heo, Y.A. Baloxavir: First Global Approval. *Drugs* **2018**, *78*, 693–697. [CrossRef] [PubMed]
2. Baxter, D. Evaluating the case for trivalent or quadrivalent influenza vaccines. *Hum. Vaccines Immunother.* **2016**, *12*, 2712–2717. [CrossRef] [PubMed]
3. Kiso, M.; Yamayoshi, S.; Murakami, J.; Kawaoka, Y. Baloxavir Marboxil Treatment of Nude Mice Infected With Influenza A Virus. *J. Infect. Dis.* **2020**, *221*, 1699–1702. [CrossRef] [PubMed]
4. Noshi, T.; Kitano, M.; Taniguchi, K.; Yamamoto, A.; Omoto, S.; Baba, K.; Hashimoto, T.; Ishida, K.; Kushima, Y.; Hattori, K.; et al. In vitro characterization of baloxavir acid, a first-in-class cap-dependent endonuclease inhibitor of the influenza virus polymerase PA subunit. *Antivir. Res.* **2018**, *160*, 109–117. [CrossRef] [PubMed]
5. Dufresne, F. Baloxavir Marboxil: An Original New Drug against Influenza. *Pharmaceuticals* **2022**, *15*, 28. [CrossRef]
6. Baloxavir Marboxil FDA Label. Available online: [https://s3-us-west-2.amazonaws.com/drugbank/cite\\_this/attachments/files/000/002/079/original/Baloxavir\\_Marboxil\\_FDA\\_label.pdf?1543256133](https://s3-us-west-2.amazonaws.com/drugbank/cite_this/attachments/files/000/002/079/original/Baloxavir_Marboxil_FDA_label.pdf?1543256133) (accessed on 16 May 2021).
7. FDA Approves New Drug to Treat Influenza. Available online: <https://www.fda.gov/news-events/press-announcements/fda-approves-new-drug-treat-influenza> (accessed on 16 May 2021).
8. Abraham, G.M.; Morton, J.B.; Saravolatz, L.D. Baloxavir: A Novel Antiviral Agent in the Treatment of Influenza. *Clin. Infect. Dis.* **2020**, *71*, 1790–1794. [CrossRef]
9. Fujita, J. Introducing the new anti-influenza drug, baloxavir marboxil. *Respir. Investig.* **2020**, *58*, 1–3. [CrossRef]
10. Taniguchi, K.; Ando, Y.; Nobori, H.; Toba, S.; Noshi, T.; Kobayashi, M.; Kawai, M.; Yoshida, R.; Sato, A.; Shishido, T.; et al. Inhibition of avian-origin influenza A(H7N9) virus by the novel cap-dependent endonuclease inhibitor baloxavir marboxil. *Sci. Rep.* **2019**, *9*, 3466. [CrossRef]
11. Takashita, E.; Ichikawa, M.; Morita, H.; Ogawa, R.; Fujisaki, S.; Shirakura, M.; Miura, H.; Nakamura, K.; Kishida, N.; Kuwahara, T.; et al. Human-to-Human Transmission of Influenza A(H3N2) Virus with Reduced Susceptibility to Baloxavir, Japan, February 2019. *Emerg. Infect. Dis.* **2019**, *25*, 2108–2111. [CrossRef]
12. Kiso, M.; Yamayoshi, S.; Furusawa, Y.; Imai, M.; Kawaoka, Y. Treatment of Highly Pathogenic H7N9 Virus-Infected Mice with Baloxavir Marboxil. *Viruses* **2019**, *11*, 1066. [CrossRef]
13. Parveen, S.; Alnoman, R.B.; Bayazeed, A.A.; Alqahtani, A.M. Computational Insights into the Drug Repurposing and Synergism of FDA-approved Influenza Drugs Binding with SARS-CoV-2 Protease against COVID-19. *Am. J. Microbiol. Res.* **2020**, *8*, 93–102.
14. Kawai, M.; Tomita, K.; Akiyama, T.; Okano, A.; Miyagawa, M. Pharmaceutical Compositions Containing Substituted Polycyclic Pyridone Derivatives and Prodrug Thereof. U.S. Patent 10,759,814, 1 September 2020.
15. Shibahara, S.; Fukui, N.; Maki, T. Method for Producing Substituted Polycyclic Pyridone Derivative and Crystal of Same. Patent WO2017221869, 28 December 2017.
16. Kawai, M. Substituted Polycyclic Pyridone Derivatives and Prodrugs Thereof. U.S. Patent 10,392,406, 27 August 2019.
17. Raw, A.S.; Furness, M.S.; Gill, D.S.; Adams, R.C.; Holcombe, F.O., Jr.; Yu, L.X. Regulatory considerations of pharmaceutical solid polymorphism in Abbreviated New Drug Applications (ANDAs). *Adv. Drug Deliv. Rev.* **2004**, *56*, 397–414. [CrossRef] [PubMed]
18. Bucar, D.K.; Lancaster, R.W.; Bernstein, J. Disappearing polymorphs revisited. *Angew. Chem. Int. Ed. Engl.* **2015**, *54*, 6972–6993. [CrossRef] [PubMed]
19. Bannigan, P.; Zeglinski, J.; Lusi, M.; O'Brien, J.; Hudson, S.P. Investigation into the Solid and Solution Properties of Known and Novel Polymorphs of the Antimicrobial Molecule Clofazimine. *Cryst. Growth Des.* **2016**, *16*, 7240–7250. [CrossRef]
20. Censi, R.; Di Martino, P. Polymorph Impact on the Bioavailability and Stability of Poorly Soluble Drugs. *Molecules* **2015**, *20*, 18759–18776. [CrossRef]
21. Li, L.; Yin, X.H.; Diao, K.S. Improving the Solubility and Bioavailability of Pemafibrate via a New Polymorph Form II. *ACS Omega* **2020**, *5*, 26245–26252. [CrossRef] [PubMed]
22. Prado, L.D.; Rocha, H.V.A.; Resende, J.A.L.C.; Ferreira, G.B.; Figueredo, T. An insight into carvedilol solid forms: Effect of supramolecular interactions on the dissolution profiles. *CrystEngComm* **2014**, *16*, 3168–3179. [CrossRef]
23. Fandaruff, C.; Rauber, G.S.; Araya-Sibaja, A.M.; Pereira, R.N.; de Campos, C.E.M.; Rocha, H.V.A.; Monti, G.A.; Malaspina, T.; Silva, M.A.S.; Cuffini, S.L. Polymorphism of Anti-HIV Drug Efavirenz: Investigations on Thermodynamic and Dissolution Properties. *Cryst. Growth Des.* **2014**, *14*, 4968–4975. [CrossRef]
24. Pudipeddi, M.; Serajuddin, A.T. Trends in solubility of polymorphs. *J. Pharm. Sci.* **2005**, *94*, 929–939. [CrossRef]

25. Sathisaran, I.; Dalvi, S.V. Engineering Cocrystals of Poorly Water-Soluble Drugs to Enhance Dissolution in Aqueous Medium. *Pharmaceutics* **2018**, *10*, 108. [CrossRef]
26. Blagden, N.; Matas, M.; Gavan, P.T.; York, P. Crystal engineering of active pharmaceutical ingredients to improve solubility and dissolution rates. *Adv. Drug Deliv. Rev.* **2007**, *59*, 617–630. [CrossRef] [PubMed]
27. Bauer, J.; Spanton, S.; Henry, R.; Quick, J.; Dziki, W.; Porter, W.; Morris, J. Ritonavir: An Extraordinary Example of Conformational Polymorphism. *Pharm. Res.* **2001**, *18*, 859–866. [CrossRef] [PubMed]
28. Singhal, D.; Curatolo, W. Drug polymorphism and dosage form design: A practical perspective. *Adv. Drug Deliv. Rev.* **2004**, *56*, 335–347. [CrossRef] [PubMed]
29. Bruker AXS Inc. Bruker AXS announces novel APEX(TM) DUO, the most versatile system for small molecule X-ray crystallography. *Anti-Corros. Methods Mater.* **2007**, *54*, 375. [CrossRef]
30. Sheldrick, G.M. SHELXT-integrated space-group and crystal-structure determination. *Acta Crystallogr. A Found Adv.* **2015**, *71*, 3–8. [CrossRef]
31. Sheldrick, G.M. Crystal structure refinement with SHELXL. *Acta Crystallogr. C Struct. Chem.* **2015**, *71*, 3–8. [CrossRef]
32. Dolomanov, O.V.; Bourhis, L.J.; Gildea, R.J.; Howard, J.A.K.; Puschmann, H. OLEX2: A complete structure solution, refinement and analysis program. *J. Appl. Crystallogr.* **2009**, *42*, 339–341. [CrossRef]
33. Macrae, C.F.; Bruno, I.J.; Chisholm, J.A.; Edgington, P.R.; McCabe, P.; Pidcock, E.; Rodriguez-Monge, L.; Taylor, R.; van de Streek, J.; Wood, P.A. Mercury CSD 2.0—new features for the visualization and investigation of crystal structures. *J. Appl. Crystallogr.* **2008**, *41*, 466–470. [CrossRef]
34. Impurities: Guideline For Residual Solvents Q3C(R5). Available online: <http://www.pmda.go.jp/files/000156308.pdf> (accessed on 17 July 1997).
35. Bojarska, J.; Fruziński, A.; Sieroń, L.; Maniukiewicz, W. The first insight into the supramolecular structures of popular drug repaglinide: Focus on intermolecular interactions in antidiabetic agents. *J. Mol. Struct.* **2019**, *1179*, 411–420. [CrossRef]
36. Qi, M.H.; Zhang, Q.D.; Liu, Y.; Ren, F.Z.; Ren, G.B. Four solid forms of filgotinib hydrochloride: Insight into the crystal structures, properties, stability, and solid-state transitions. *J. Mol. Struct.* **2019**, *1178*, 242–250. [CrossRef]
37. Spackman, P.R.; Turner, M.J.; McKinnon, J.J.; Wolff, S.K.; Grimwood, D.J.; Jayatilaka, D.; Spackman, M.A. CrystalExplorer: A program for Hirshfeld surface analysis, visualization and quantitative analysis of molecular crystals. *J. Appl. Cryst.* **2021**, *54*, 575–587. [CrossRef] [PubMed]
38. Bavishi, D.D.; Borkhataria, C.H. Spring and parachute: How cocrystals enhance solubility. *Prog. Cryst. Growth Charact. Mater.* **2016**, *62*, 1–8. [CrossRef]
39. Chu, K.R.; Lee, E.; Jeong, S.H.; Park, E.S. Effect of particle size on the dissolution behaviors of poorly water-soluble drugs. *Arch. Pharmacol Res.* **2012**, *35*, 1187–1195. [CrossRef]
40. Destri, L.G.; Marrazzo, A.; Rescifina, A.; Punzo, F. How molecular interactions affect crystal morphology: The case of haloperidol. *J. Pharm. Sci.* **2011**, *100*, 4896–4906. [CrossRef] [PubMed]
41. Mishnev, A.; Stepanovs, D. Crystal Structure Explains Crystal Habit for the Antiviral Drug Rimantadine Hydrochloride. *Z. Nat. B* **2014**, *69*, 823–828. [CrossRef]
42. Xu, T.; Jiang, Z.; He, M.; Gao, X.; He, Y. Effect of arrangement of functional groups on stability and gas adsorption properties in two regioisomeric copper bent diisophthalate frameworks. *CrystEngComm* **2019**, *21*, 4820–4827. [CrossRef]
43. Modi, S.R.; Dantuluri, A.K.R.; Perumalla, S.R.; Sun, C.C.; Bansal, A.K. Effect of Crystal Habit on Intrinsic Dissolution Behavior of Celecoxib Due to Differential Wettability. *Cryst. Growth Des.* **2014**, *14*, 5283–5292. [CrossRef]
44. Kumar, D.; Thipparaboina, R.; Shastri, N.R. Can vacuum morphologies predict solubility and intrinsic dissolution rate? A case study with felodipine polymorph form IV. *J. Comput. Sci.* **2015**, *10*, 178–185. [CrossRef]
45. Chen, J.; Trout, B.L. Computer-Aided Solvent Selection for Improving the Morphology of Needle-like Crystals: A Case Study of 2,6-Dihydroxybenzoic Acid. *Cryst. Growth Des.* **2010**, *10*, 4379–4388. [CrossRef]
46. Moreno-Calvo, E.; Calvet, T.; Cuevas-Diarte, M.A.; Aquilano, D. Relationship between the Crystal Structure and Morphology of Carboxylic Acid Polymorphs. Predicted and Experimental Morphologies. *Cryst. Growth Des.* **2010**, *10*, 4262–4271. [CrossRef]
47. Jha, K.K.; Dutta, S.; Kumar, V.; Munshi, P. Isostructural polymorphs: Qualitative insights from energy frameworks. *CrystEngComm* **2016**, *18*, 8497–8505. [CrossRef]
48. Mackenzie, C.F.; Spackman, P.R.; Jayatilaka, D.; Spackman, M.A. CrystalExplorer model energies and energy frameworks: Extension to metal coordination compounds, organic salts, solvates and open-shell systems. *IUCr* **2017**, *4*, 575–587. [CrossRef] [PubMed]
49. Turner, M.J.; Thomas, S.P.; Shi, M.W.; Jayatilaka, D.; Spackman, M.A. Energy frameworks: Insights into interaction anisotropy and the mechanical properties of molecular crystals. *Chem. Commun.* **2015**, *51*, 3735–3738. [CrossRef] [PubMed]